Extraction of local coordination structure in a low-concentration uranyl system by XANES

Linjuan Zhang,[a]* Jing Zhou,[a] Jianyong Zhang,[a] Jing Su,[a] Shuo Zhang,[a] Ning Chen,[b] Yunpeng Jia,[a] Jiong Li,[a] Yu Wang[a] and Jian-Qiang Wang[a]*

[a]Shanghai Institute of Applied Physics, Chinese Academy of Sciences, Shanghai 201800, People's Republic of China, and [b]Canadian Light Source, Saskatoon, Saskatchewan, Canada S7N 2V3.
*Correspondence e-mail: zhanglinjuan@sinap.ac.cn, wangjianqiang@sinap.ac.cn

Obtaining structural information of uranyl species at an atomic/molecular scale is a critical step to control and predict their physical and chemical properties. To obtain such information, experimental and theoretical L_3-edge X-ray absorption near-edge structure (XANES) spectra of uranium were studied systematically for uranyl complexes. It was demonstrated that the bond lengths (R) in the uranyl species and relative energy positions (ΔE) of the XANES were determined as follows: $\Delta E_1 = 168.3/R(U-O_{ax})^2 - 38.5$ (for the axial plane) and $\Delta E_2 = 428.4/R(U-O_{eq})^2 - 37.1$ (for the equatorial plane). These formulae could be used to directly extract the distances between the uranium absorber and oxygen ligand atoms in the axial and equatorial planes of uranyl ions based on the U L_3-edge XANES experimental data. In addition, the relative weights were estimated for each configuration derived from the water molecule and nitrate ligand based on the obtained average equatorial coordination bond lengths in a series of uranyl nitrate complexes with progressively varied nitrate concentrations. Results obtained from XANES analysis were identical to that from extended X-ray absorption fine-structure (EXAFS) analysis. XANES analysis is applicable to ubiquitous uranyl–ligand complexes, such as the uranyl–carbonate complex. Most importantly, the XANES research method could be extended to low-concentration uranyl systems, as indicated by the results of the uranyl–amidoxime complex ($\sim$40 p.p.m. uranium). Quantitative XANES analysis, a reliable and straightforward method, provides a simplified approach applied to the structural chemistry of actinides.

1. Introduction

As the most important component of nuclear fuel, uranium occurs in four different oxidation states (Vitova *et al.*, 2010, 2013) as follows: U^{3+} (U[III]), U^{4+} (U[IV]), UO^{2+} (U[V]) and UO_2^{2+} (U[VI]/uranyl ion); it easily forms various molecular structures with different ligands, which directly determine macroscopic physical and chemical properties (Altmaier *et al.*, 2013; Geckeis *et al.*, 2013; Knope & Soderholm, 2013). Generally, the structural chemistry of the uranyl ion (UO_2^{2+}) is central to the reprocessing of nuclear waste, sequestration of uranium from seawater, and analysis of the effects of uranium on the environment and geosphere (Berto *et al.*, 2012; Stoliker *et al.*, 2013; Kim *et al.*, 2013). The uranyl ion has axial trans-dioxo atoms in the apical position and equatorial coordination geometry bound to the surrounding ligands (*e.g.* carbonate or nitrate), thereby forming a complex ligand species (Walshe *et al.*, 2014; Gaillard *et al.*, 2012; Pemberton *et al.*, 2013). In a solution system, the coordination structure of uranyl complexes is mainly controlled by concentration, pH and temperature (Bailey *et al.*, 2005; Gückel *et al.*, 2013; Hennig *et*

Uranyl ions samples
— in 1M HClO$_4$
— in 4M HNO$_3$
— in 7M HNO$_3$
— in 10M HNO$_3$
— uranyl nitrate solid

ABSORPTION (arb.unit)

$\Delta E_1 = 168.3/R(U-O_{ax})^2-38.5$
$\Delta E_2 = 428.4/R(U-O_{eq})^2-37.1$

Energy (eV)
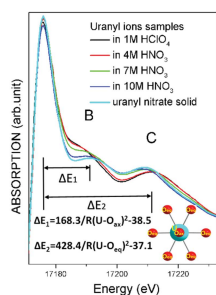
al., 2007). Understanding the structure of uranyl species at an atomic/molecular scale is a critical step in controlling and predicting their physical and chemical properties. Several different techniques have been applied to investigate uranyl compounds (Moulin *et al.*, 1995; Denecke, 2006; De Houwer & Görller-Walrand, 2001), such as time-resolved laser-induced fluorescence spectroscopy, UV–vis, IR, Raman and X-ray absorption fine-structure (XAFS) spectroscopy. XAFS has been widely recognized as a powerful characterization technique for molecular and electronic structures in uranium chemistry based on the following reasons: (i) element-specificity allows the extraction of structural information of the uranium element from other coexisting metal elements; (ii) structural information can be obtained from complex solution systems (*e.g.* water, organic solution or molten salts), solid systems (*e.g.* natural sediments or silica gels) and biological systems; and (iii) the high penetration depth of the high photon energies in the uranium L_3 absorption edge ($\sim$17166 eV) can probe radioactive samples with specific protection containment (Denecke, 2006; Polovov *et al.*, 2008; Den Auwer *et al.*, 2003). In the XAFS technique, extended X-ray absorption fine-structure (EXAFS) oscillations provide metrical parameters that describe short-range order surrounding the absorbing atom and quantitative structural information, such as bond length (R), coordination number (CN) and Debye–Waller factor (σ^2). Therefore, most reports (Den Auwer *et al.*, 2003; Hennig *et al.*, 2007; Polovov *et al.*, 2008; Ikeda *et al.*, 2007; Visser *et al.*, 2003) about the molecular structure of uranium systems are mainly based on this method. However, for dilute systems, EXAFS measurements require rigorous experimental conditions to acquire high-quality data, *i.e.* high-flux light source and stable monochromator. In particular, it usually takes a long time to collect data and as a result radiation damage of the complex is an unavoidable problem. Recently, Chantler *et al.* (2015) proposed a hybrid technique using transmission XAS to extract accurate coordination information in mM solutions. However, as they reported, for a weak 1.5 mM solution only XANES and low-energy EXAFS data can be used. As the concentration further decreases, it will no longer be sufficient to extract quantitative structure information. By contrast, XANES is a more appropriate detection tool that can easily obtain relatively high quality data, because its intensity is more than 100 times stronger than that of the EXAFS signal ($k \simeq 10$). Due to the larger photoelectron scattering cross section compared with that of the EXAFS signal, multiple-scattering paths must be included in the simulation of XANES spectra. At the time of writing, no straightforward equation such as EXAFS analysis has been found to directly extract quantitative structural information from XANES data. A significant XANES quantitative approach (the *MXAN* procedure) (Benfatto & Della Longa, 2001; Natoli & Benfatto, 1986) has been proposed for deriving the geometrical information by fitting the experimental spectrum and several theoretical calculations generated by changing relevant geometrical parameters of the site around the absorbing atom, which play an important role in biological systems (Yang *et al.*, 2008; Zhang, Yan *et al.*, 2010),

but the spectrum calculations are time-consuming. On the basis of XANES fitting, Smolentsev & Soldatov (2006, 2007) explored the *FitIt* software using multi-dimensional interpolation of spectra with a limited number of multiple-scattering calculations. Bugaev *et al.* (2001) proposed to use Fourier filtration of XANES to obtain the same structural information as in classical EXAFS, but this method has been demonstrated only for crystalline compounds and minerals consisting of low-Z elements (Bugaev *et al.*, 1998, 2000) and application to other systems are still unknown. Theoretical calculations (such as quantum chemistry and molecular dynamics) have also been applied to explain the XANES characters (D'Angelo *et al.*, 2010; Conradson *et al.*, 2004; Den Auwer *et al.*, 2004), but the systematic study of XANES data in the uranyl complex is still possible and necessary.

Extracting qualitative structural information, such as bond lengths, from the uranium L_3-edge XANES spectrum is an important step in extending XAFS research on lower uranyl concentration systems. In the chemisorbed low-Z molecules, transition-metal oxides and rare-earth complexes (Joseph *et al.*, 2009; Bianconi *et al.*, 1985; Stöhr *et al.*, 1983) the effect of the interatomic distance R has been shown to shift the multiple-scattering resonances in the XANES spectrum, following the Natoli rule $\Delta E \times R^2$ = constant. In the high-valence actinide system, some groups have carried out good research using the XANES technique, and the double-peaked structure in the L_3-edge XAFS of higher formal U valence raises long-term controversy about the origin of multiple scattering (Hudson *et al.*, 1995; Petiau *et al.*, 1986; Kalkowski *et al.*, 1987) or multi-electronic configuration (Bertram *et al.*, 1989; Kaindl *et al.*, 1987, 1988; Kalkowski *et al.*, 1988). But there is no doubt about the certain relationship between the shape resonance and the bond lengths (Den Auwer *et al.*, 2003; Jollivet *et al.*, 2002; Petiau *et al.*, 1986). However, the exact values of the constant, which would obviously simplify and facilitate the extraction of structural data, have not been given. Thus, we conducted a systematic experimental and theoretical study on the uranium L_3-edge XANES feature in the uranyl complex. In this study, we constructed a research method to obtain qualitative structural information from XANES analysis, and demonstrated the direct relationship between the bond length and XANES features. We used uranyl nitrate as the model molecule, which contains a typical uranyl coordination unit. Local structural data of the uranyl nitrate solid were initially confirmed by X-ray diffraction (XRD) and EXAFS fits, and used to establish a relationship between the bond length and XANES feature *via* XANES simulations and the linear combination least-squares fit method. Based on this relationship, the axial and equatorial coordination average bond lengths around the uranium atom in a series of uranyl nitrate complexes, as well as in the $(NH_4)_4UO_2(CO_3)_3$ solid, were obtained. The reliability of the XANES results was also verified with the EXAFS fits. Finally, we demonstrated that our research method based on XANES analysis could be applied to explore the local structural environment in relatively low concentration uranium systems.

research papers

2. Experiment and calculations

Uranyl-nitrate solutions. All samples were prepared from $UO_2(NO_3)_2 \cdot 6H_2O$ solid, which was dissolved in aqueous solutions with the required $HClO_4$ or HNO_3 concentration. In each sample, the U concentration was maintained at 0.04 *M*. The $HClO_4$ concentration was 1 *M*. The nitrate concentration was adjusted to 4, 7 or 10 *M*.

Synthesis of $(NH_4)_4UO_2(CO_3)_3$. $UO_2(NO_3)_2 \cdot 6H_2O$ (0.007 mol) was directly dissolved in a specific amount of deionized water. Subsequently, $(NH_4)_2CO_3$ aqueous solutions (0.12 mol) were slowly dropped into the uranyl nitrate solution. Yellow precipitate $[(NH_4)_4UO_2(CO_3)_3]$ was isolated by centrifugation and collected after drying.

Preparation of the uranyl–amidoxime complex. Fibrous amidoxime adsorbent was prepared according to the method reported by Liu *et al.* (2012). Uranyl ion adsorption was performed with initial U concentrations of 50 p.p.b. at pH 7.5 and then stored for one week. The final adsorption amount of uranyl ion concentration was determined at about 40 p.p.m. by inductively coupled plasma mass spectrometry.

X-ray absorption fine-structure data were collected at beamline 14W of the Shanghai Synchrotron Radiation Facility with a Si(111) double-crystal monochromator in transmission and fluorescence modes for the uranium L_3-edge spectra. The electron beam energy of the storage ring was 3.5 GeV, and the maximum stored current was approximately 210 mA. The energy calibration was performed using a Zr foil ($\sim$17998 eV). Each sample was measured three times and the spectra averaged. The U L_3-edge XAFS data were analysed using standard procedures in *Demeter* (Ravel & Newville, 2005). The normalized uranium L_3-edge X-ray absorption spectra of all uranyl species are shown in Fig. S1 of the supporting information. The double-electron excitations affect the EXAFS signal and can influence the result of data analysis (Hennig, 2007; Gomilšek *et al.*, 2003; Benfield *et al.*, 1994; Kodre *et al.*, 2002). Thus, in uranium L_3-edge EXAFS experimental spectra the double-electron excitations were subtracted as a reflection of the data translated to the position in energy of the excitation using the standard procedures in *Demeter*. Figure S2 of the supporting information shows the uranium L_3-edge EXAFS data before and after subtracting the double-electron excitation in *k*- and *R*-space, in which the feature at very low distances ($R \simeq 1$ Å) obviously improved. Theoretical phase and amplitude functions were calculated using *FEFF9.0* (Rehr *et al.*, 2010). The amplitude reduction factor S_0^2 was fixed at 0.9 in EXAFS fits, and the shifts in the threshold energy ΔE_0 were constrained to be the same value for all fitted shells. In consideration of the large correlation between CN and Debye–Waller parameters (σ^2), we fixed the σ^2 values for the uranyl nitrate sample system to the estimated values for the uranyl ions in 1 *M* $HClO_4$ solution.

XANES simulations were performed in the framework of multiple-scattering (MS) theory (Lee & Pendry, 1975) using *FEFF9.0*. The cluster potential was estimated by a set of spherically averaged muffin-tin potentials. The *FEFF* input file was generated using the *ATOM* package. For calculations, we used the Hedin–Lundqvist model (Natoli *et al.*, 1990; Tyson *et al.*, 1992). To evaluate the credibility of the calculated spectra, a model cluster size of up to 95 atoms was used in the MS calculations of $UO_2(NO_3)_2(H_2O)_2$ solid to obtain an accurate self-consistent field (SCF) calculation while a larger cluster (200 atoms) was used for full multiple-scattering (FMS) calculations. Multiple-scattering contributions from different cluster sizes were calculated to explore the origin of the multiple-scattering features referred to in previous works (Wu *et al.*, 1997; Xu *et al.*, 2011; Zhang, Zhang *et al.*, 2010). We also performed XANES calculations using the *FDMNES* code (Joly, 2001) within both the muffin-tin and FDM models for comparison (Fig. S3). XANES calculations were performed based on the structural model of $UO_2(NO_3)_2(H_2O)_2$ ($Cmc2_1$, ICSD-23825), as indicated by the XRD result. Linear combination least-squares fit modelling of the U L_3-edge XANES spectra was performed with *WinXAS* (Ressler, 1998) utilizing three pseudo-Voigt $[f(x) = \alpha\text{Gaussian} + (1 - \alpha)\text{Lorentzian}]$ and one arctangent line shapes (Vitova *et al.*, 2010; Walshe *et al.*, 2014). The arctangent curve shows the transitions from U $2p_{3/2}$ to the continuum and thus reflects the absorption-edge jump, whose position was determined at the maximum of the first derivative of the white line (WL).

3. Results and discussion

3.1. Establishing the relationship between the local structure and XANES features

To establish an accurate relationship between the XANES features and local structure, we selected a typical standard sample $UO_2(NO_3)_2(H_2O)_2$ ($Cmc2_1$, ICSD-23825) as a reference, in which the coordination polyhedron of the uranyl complex can be described as a bipyramid with the axial trans-dioxo atoms (O_{ax}) in the apical position and equatorial coordination oxygen geometry (O_{eq}) from two water molecules and two nitrate ligands, as shown in the inset of Fig. S4 of the supporting information. Local structural information was expected to be determined by U L_3-edge EXAFS analysis of the $UO_2(NO_3)_2(H_2O)_2$ solid. The collected EXAFS spectra (k^3-weighted) and their corresponding Fourier transforms (FTs) are shown in Figs. 1(*a*) and 1(*b*). Clear EXAFS oscillation patterns were observed at up to $k = 20$ Å^{-1} for the $UO_2(NO_3)_2(H_2O)_2$ solid. Compared with the scattering contribution from different paths near the absorber atom based on the model of ICSD-23825 shown in Fig. 1(*a*), we could clearly observe the effect of U—O_{eq} from the water molecule (P1, P3 and P4) and nitrate ligand (P2 and P5). According to path analysis in *R*-space based on the model of ICSD-23825 shown in Fig. 1(*b*), we assigned the peaks at *R* values of 1.5 (A), 2.0 (B) and 2.1 Å (C) to the single-scattering (SS) paths of O_{ax}, $O_{eq}(H_2O)$ and $O_{eq}(NO_3)$, respectively. The superposition of peaks A and B produced an additional FT peak between them ($R \simeq 1.7$ Å), although it cannot be used directly from a structure assignment perspective (Ikeda-Ohno *et al.*, 2008, 2009). Quantitative information obtained from
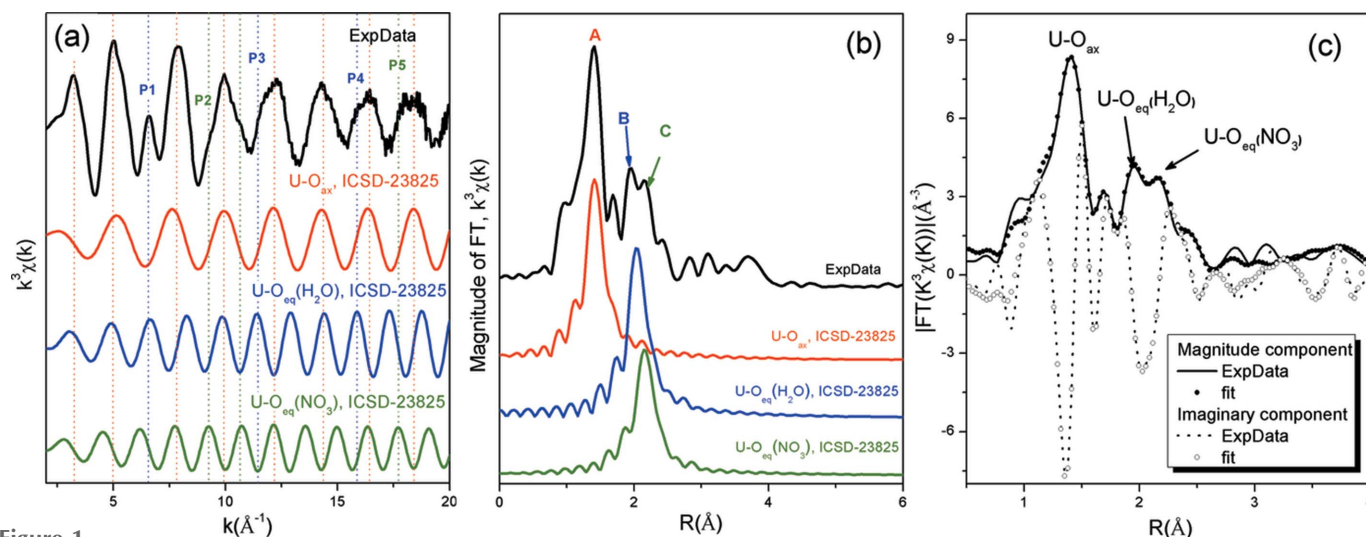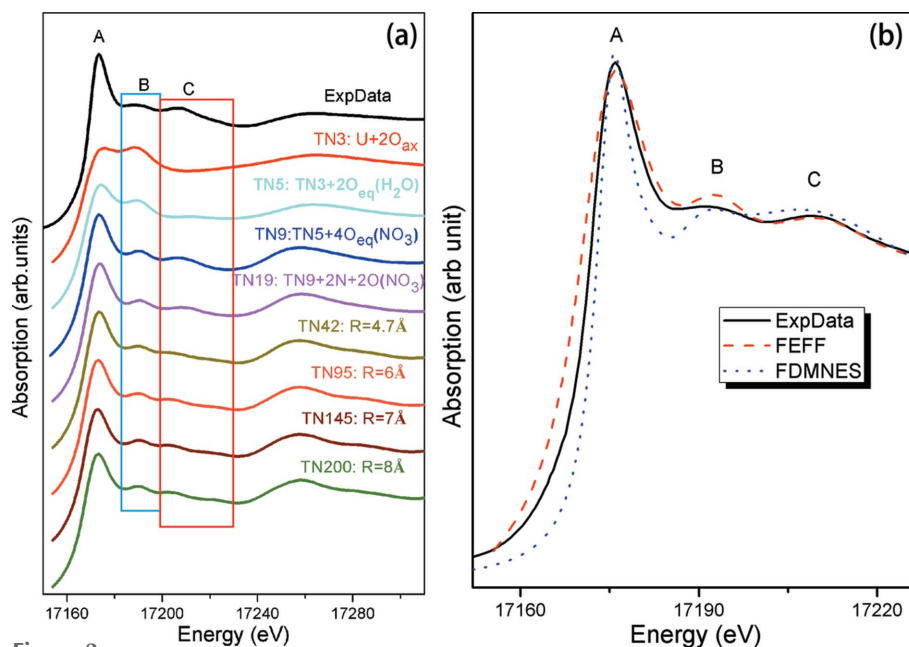
Figure 1
(*a, b*) *k*-Weighted EXAFS $\chi(k)$ function and its corresponding Fourier transform (FT) for the uranium L_3-edge for the $UO_2(NO_3)_2(H_2O)_2$ experimental data after subtracting the double-electron excitation are shown at the top of each panel (black trace). Beneath the experimental data are the contributions from each individual path of the standard model of ICSD-23825. (*c*) Magnitude and imaginary components of the FT for the experimental data of the $UO_2(NO_3)_2(H_2O)_2$ powder sample and corresponding fits.

EXAFS fits is shown in Fig. 1(*c*) and Table S1, in which values for *R* had an accuracy of ± 0.02 Å. The interatomic distances of the uranyl nitrate solid in the primary coordination sphere, namely $U-O_{ax}$, $U-O_{eq}(H_2O)$ and $U-O_{eq}(NO_3)$, were 1.75, 2.39 and 2.50 Å, respectively. Notably, the distance of $U-O_{eq}(NO_3)$ was longer than that of $U-O_{eq}(H_2O)$ by 0.11 Å, which may be due to water molecules forcing the nitrate away from the uranyl (Siboulet *et al.*, 2006; de Jong *et al.*, 2005). $CN(U-O_{eq})$ in its equatorial plane is close to 6, although relatively large errors are always known when determining the CN, which ranges from 10% to 25% in the EXAFS fits (Ikeda-Ohno *et al.*, 2008; Sandström *et al.*, 2001; Hennig, 2007) due to double-electron excitation or strong correlation between CN and the Debye–Waller factors. Compared with the reference ICSD-23825 model, higher degeneration of scattering paths obtained by EXAFS analysis was considered in the $UO_2(NO_3)_2(H_2O)_2$ sample for further analysis.

After confirming the structure from EXAFS and XRD analysis, we explored the XANES features affected by the local environment in the $UO_2(NO_3)_2$-$(H_2O)_2$ solid. As shown in the top curve of Fig. 2(*a*), typical XANES in the $UO_2(NO_3)_2(H_2O)_2$ solid displayed a strong WL (A), a shoulder (B) at about 15 eV, and a feature (C) at 35 eV above the WL maximum. The fine structure around the absorption edge generally comprises the contribution from the

electron transitions into atom-like orbitals and MS features. To distinguish the origin of feature peaks and recognize MS contributions from different shells in the U L_3-edge XANES spectrum, we carried out calculations using different atomic clusters around the uranium absorber in the $UO_2(NO_3)_2(H_2O)_2$ solid, as shown in Fig. 2(*a*). For a cluster with uranium as the central atom, the first shell consisting of the axial trans-dioxo atoms reproduced peak B. After the

Figure 2
(*a*) Comparison of MS calculations for different atomic clusters of the uranium L_3-edge for the $UO_2(NO_3)_2(H_2O)_2$ solid based on the *FEFF* code. TN reflects the total atom number. (*b*) Comparison of experimental and theoretical uranium L_3-edge XANES spectra in the $UO_2(NO_3)_2(H_2O)_2$ solid. The *FEFF* spectrum corresponds to the TN9 model. The *FDMNES* spectrum corresponds to the result based on the FDM model, which is more precise than that based on the muffin-tin approximation, as shown in Fig. S3.

addition of two oxygen atoms from the H_2O molecule in the equatorial coordination, the intensity of peaks A and C increased slightly, whereas peak B was almost unaffected. Further inclusion of the equatorial oxygen atoms from the NO_3^- group, corresponding to nine atoms, resulted in a sharpening of feature A and the pattern of peak C was reproduced. A continuous increase in the cluster size (up to 8 Å) did not induce further changes in XANES patterns, which implies that the model of nine atoms was sufficient to reproduce all features of the experimental spectrum in this study. In Fig. 2(b) the U L_3-edge XANES spectra calculated by *FEFF9.0* and *FDMNES* showed that the corresponding spectral features were quite comparable, but the results by *FEFF* code gave a better agreement with the experimental spectra in this system. Thus, the following simulations were mainly based on *FEFF*. Given the dipole selection rules, electronic transitions appearing in the XANES spectrum at the U L_3-edge were dominated by transitions from $2p_{3/2}$ to d-like empty states. On the basis of MS calculations, peaks B and C were directly correlated with the axial oxygen atoms (U—O_{ax}) and equatorial oxygen atoms (U—O_{eq}), respectively. The obtained MS paths were analogous to Templeton's and Hudsons' research based on the polarized XAS measurements (Templeton & Templeton, 1982; Hudson *et al.*, 1995, 1996). The energy positions of two continuum reso-

nance peaks B and C depend on the U—O_{ax} and U—O_{eq} distances, respectively, which change between compounds with the same valence but different constituents in the equatorial bonding plane (Denecke, 2006; Vitova *et al.*, 2010).

To quantify the feature changes in the edge position, two series of simulations using *FEFF9.0* were carried out using similar parameters as mentioned previously. In simulation I, the axial bonds were elongated from 1.71 Å to 1.81 Å with the equatorial bonds from the contribution of the H_2O and NO_3 ligands fixed at distances of 2.39 and 2.50 Å, respectively, as referred to in the results of EXAFS fitting. In simulation II, the equatorial bond of U—$O_{eq}(NO_3)$ was shortened from 2.52 Å to 2.39 Å, whereas the bond lengths of U—$O_{eq}(H_2O)$ and U—O_{ax} were maintained at fixed distances of 2.39 and 1.75 Å, respectively. The systematic shifts of the continuum resonance peaks B and C were qualitatively reproduced with the bond length of U—O_{ax}/O_{eq} by the simulations in Figs. 3(a) and 3(b), respectively. The detailed energy positions of each curve were analysed by least-squares fitting (Fig. S5), and the qualitative results of energy separation of the two continuum resonance peaks B and C with respect to the WL (ΔE) are listed in Table S2. The energy separation (ΔE) as a function of $1/R^2$ is displayed in Figs. 3(c) and 3(d), showing a linear increase with $1/R^2$ as expected. To quantitatively describe the
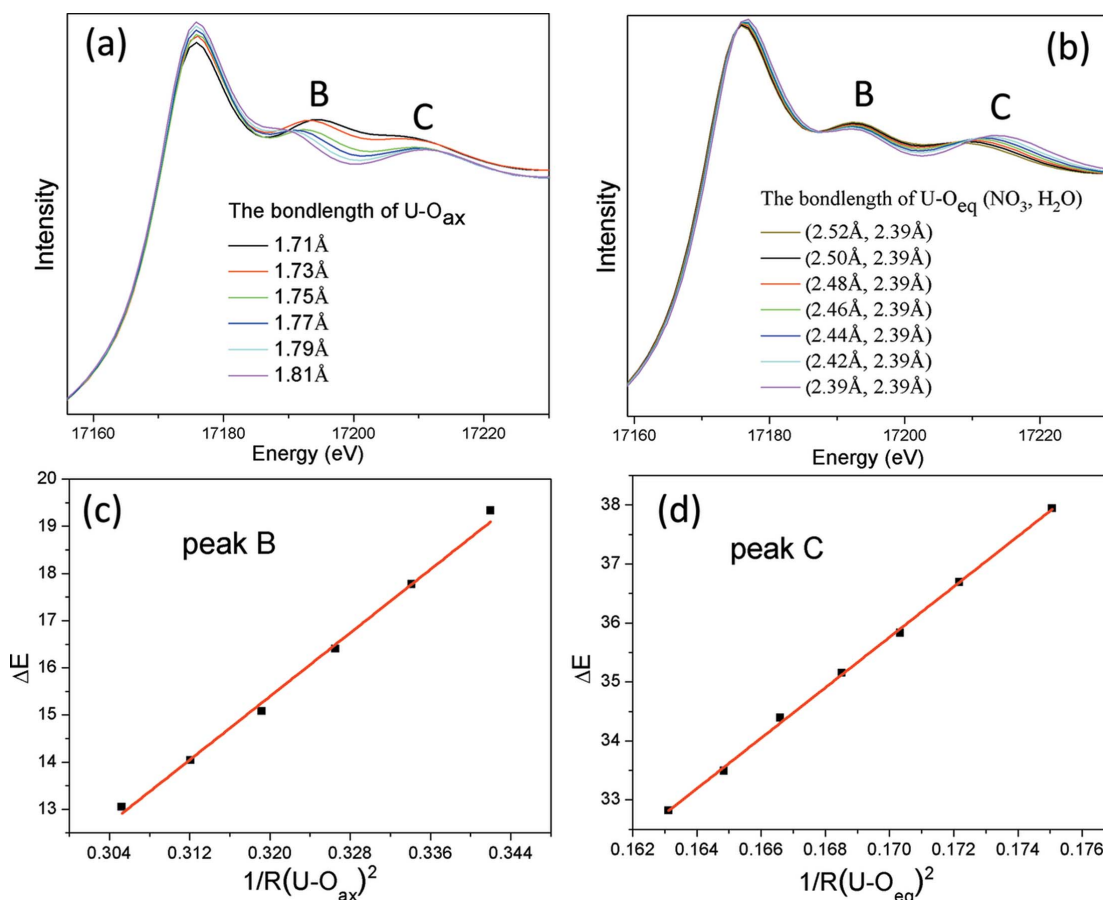

Figure 3
Comparison of theoretical XANES spectra with varying bond lengths of U—O_{ax} (a) and U—O_{eq} (b). (c, d) The linear relation between ΔE and $1/R^2$. ΔE indicates energy separation between the WL and continuum resonance peak B or C. Red lines correspond to the linear fitting curve.

relationship between ΔE and $1/R^2$, curve fitting was employed with the model as follows:

Function 1 : $\quad \Delta E_1 = 168.3/R(\text{U} - \text{O}_{ax})^2 - 38.5$ (peak B),

Function 2 : $\quad \Delta E_2 = 428.4/R(\text{U} - \text{O}_{eq})^2 - 37.1$ (peak C),

in which the error of linear fitting for Functions 1 and 2 are about 168.3 ± 0.4, 38.5 ± 0.1 and 428.4 ± 1.3, 37.1 ± 0.2, respectively.

For uranyl solutions, only short-range interactions need to be considered. Unlike other systems (Chen *et al.*, 2013), the first and second peaks after the WL may be related to crystallinity. In the dilute uranyl systems, the total intensity axial trans-dioxo atoms and equatorial coordination atoms were sufficient to reproduce the continuum resonance peaks B and C very well.

As we know, uranyl ions have axial trans-dioxo atoms in the apical position and equatorial coordination geometry bound to the surrounding ligands. Thus these uranyl compounds have similar geometry structure in the oxidation state +6, and thus the U—O bond length changes in an acceptable range of $\pm 10\%$. According to previous references (Bailey *et al.*, 2005; Schlegel & Descostes, 2009; Hennig *et al.*, 2005; Denecke *et al.*, 1998; Shi *et al.*, 2014), in the uranyl–ligand complex the bond lengths of U—O$_{ax}$ and U—O$_{eq}$ mostly lie in the range 1.75–1.82 and 2.29–2.53 Å, respectively, which are strongly related to the ligand type (such as OH$^-$, CO$_3^{2-}$ and PO$_4^{3-}$) and environmental conditions (pH and temperature). The accu-

racy of XANES analysis needs to be evaluated carefully. According to the law of propagation of error, the error of distance in the XANES relationship formula depends on the error of ΔE and curve linear fitting (Vitova *et al.*, 2010). On the basis of the above evaluation, the error of bond length in the axial and equatorial planes determined by XANES analysis was within 0.01 Å, which was comparable with that of EXAFS fitting.

3.2. Determining the local structures of the uranyl ion in solution by XANES analysis

In principle, based on the above empirical functions, which link the local coordination structure and XANES feature in the uranyl systems, we can directly calculate the bond distance around the uranium absorber by simply fitting the experimental XANES spectra of the samples. A series of uranyl nitrate complexes was selected to verify our method. U L_3-edge XANES spectra of UO$_2^{2+}$ in HClO$_4$ or HNO$_3$ aqueous solutions were collected and normalized, as shown in Fig. 4(a). Two main observations were obtained. (i) Line shapes were consistent between UO$_2^{2+}$ in HClO$_4$ or different HNO$_3$ solutions compared with the UO$_2$(NO$_3$)$_2$(H$_2$O)$_2$ solid, which implies that the bipyramid skeletal structure was maintained. (ii) The energy separation between peaks B and C was larger in these uranyl solutions compared with that observed in the solid sample. On the one hand, as a general belief that perchlorate ions cannot coordinate with the cation in aqueous
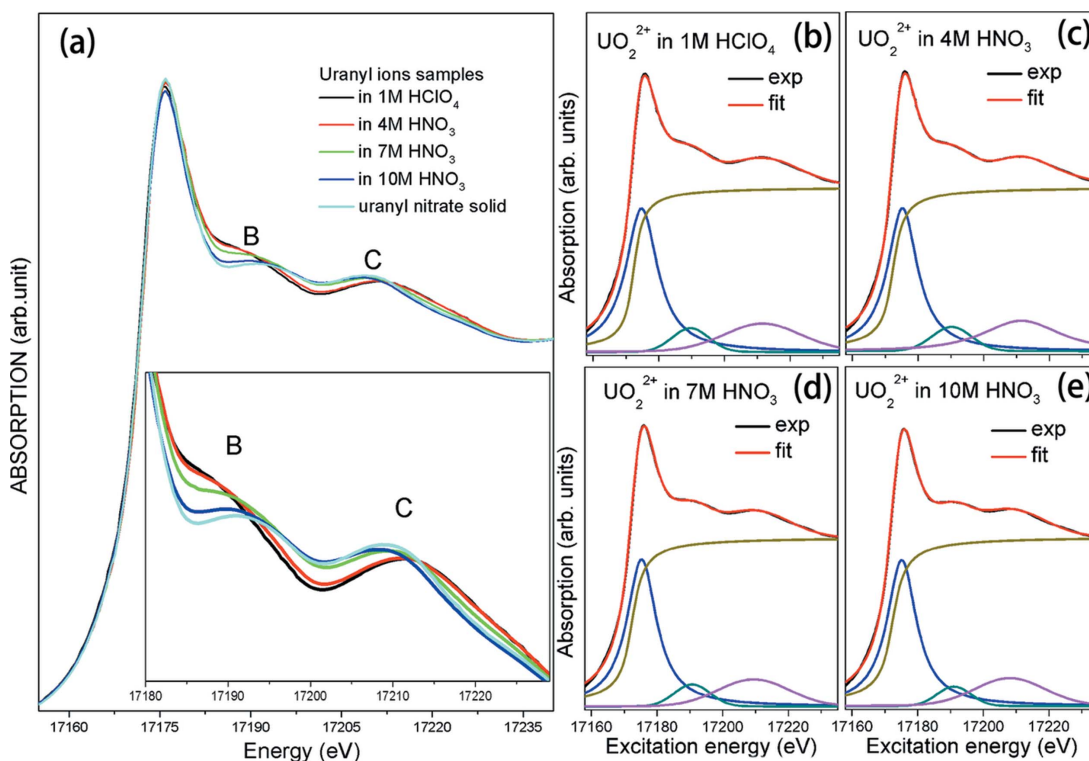

Figure 4
(a) Comparison of experimental L_3-edge XANES spectra collected from uranyl ions in HClO$_4$ and solution samples with different HNO$_3$ concentrations, as well as the UO$_2$(NO$_3$)$_2$(H$_2$O)$_2$ solid powder. The zoomed inset shows the continuum MS resonance regions. (b)–(e) The experimental L_3-edge XANES spectra and their pseudo-Voigt line shapes determined by least-squares fitting of linear combination analyses for uranyl ions in different solutions.

solutions because of its weak coordination ability, the uranyl ion in the perchlorate acid solution is surrounded by pure hydrate molecule. On the other hand, with the increase in nitrate concentration, the gradual shape variation implies that the nitrate ligand may gradually substitute the hydrate molecule. The pattern of the U L_3-edge XANES transformed from initially similar to the pattern in the $HClO_4$ solution to that in the $UO_2(NO_3)_2(H_2O)_2$ solid when the nitrate concentration increased to 10 M.

To obtain exact local structural information, the energy positions of continuum scattering peaks of the U L_3-edge XANES parts in different uranyl samples were analysed by least-squares fitting [Figs. 4(b)–4(e)], and the results are listed in Table S2. According to the above-determined linear equation between R and ΔE [Function 1: $\Delta E_1 = 168.3/R(U-O_{ax})^2 - 38.5$ for peak B; Function 2: $\Delta E_2 = 428.4/R(U-O_{eq})^2 - 37.1$ for peak C], we could directly obtain the uranyl coordination structure for uranyl ions in 1 M $HClO_4$, 4 M HNO_3, 7 M HNO_3 and 10 M HNO_3 from XANES analysis. The calculated $U-O_{ax}$ bond distances in 1 M $HClO_4$, 4 M HNO_3, 7 M HNO_3 and 10 M HNO_3 were 1.78 ± 0.01, 1.77 ± 0.01, 1.77 ± 0.01 and 1.76 ± 0.01 Å, respectively, whereas the average bond distances of $U-O_{eq}$ were 2.41 ± 0.01, 2.42 ± 0.01, 2.45 ± 0.01 and 2.47 ± 0.01 Å, respectively.

The equatorial oxygen ligands for uranyl ions in different HNO_3 solutions had two possible sources, namely nitrate groups and water molecules. The EXAFS fitting results in the $UO_2(NO_3)_2(H_2O)_2$ solid revealed that the bond length of $U-O_{eq}(NO_3)$ was longer than that of $U-O_{eq}(H_2O)$ by up to 0.11 Å. In a series of uranyl nitrate solutions, the gradual increase in average bond length of $U-O_{eq}$ was mainly attributed to more oxygen coordination atoms from the water molecule replaced by the nitrate ligand with increasing concentration of nitric acid. Thus, we could estimate the relative weight of the oxygen ligand derived from the nitrate ligand and water molecule in different uranyl nitrate complexes. Considering the accuracy of EXAFS detection and the effect of hydration in the aqueous solution (Bühl et al., 2006; Hagberg et al., 2005), we cannot distinguish the bond length within 0.02 Å and the CN of 5–6. In this estimation, we set the bond length of $U-O_{eq}(H_2O)$ and $U-O_{eq}(NO_3)$ at 2.39 and 2.50 Å, respectively, and assumed that the total CN in the equatorial plane was always 6. According to the following equation,

$$6 \times R_{ave}(U - O_{eq}) = CN \times R_{H2O}(U - O_{eq}) + (6 - CN) \times R_{NO3}(U - O_{eq}),$$

the relative weights of coordinated oxygen derived from water and nitrate ligand in 4, 7 and 10 M HNO_3 were approximately 4.4:1.6, 2.7:3.3 and 1.6:4.4, respectively. The accuracy of this evaluation was limited by the error of bond length fitting and fluctuations of total CN (5–6) in the equatorial plane, but this result could still be used as a reference for further theoretical research. The sensitivity of XANES analysis to the CN has also been reported using the K-edge XANES spectra by Bugaev et al. (2000, 2001). Therefore, quantitative local

structural information could be obtained by analysing the U L_3-edge XANES spectra. Moreover, XANES features were easy to collect and highly available for low-concentration samples compared with the EXAFS data.

3.3. Reliability of XANES analysis by comparison with EXAFS analysis

Given that the above-established equations were based on the theoretical XANES simulations, the reliability of these functions need to be verified by comparing quantitative information about the local structures with results from EXAFS fitting for the different uranyl nitrate solution samples. The collected EXAFS spectra (k^3-weighted) and their corresponding FTs are shown in Figs. 5(a) and 5(b), in which significant feature changes, marked by pink arrows, are illustrated in both k- and R-space data. Referred to the path assigned in R-space of the $UO_2(NO_3)_2(H_2O)_2$ solid, peaks at R values of 1.5, 2.0 and 2.1 Å corresponded to the SS paths of O_{ax}, $O_{eq}(H_2O)$ and $O_{eq}(NO_3)$, respectively. With the increase in HNO_3 concentration, the following changes were observed: (i) a subtle position change was detected for peak A, which reflected the decrease in bond length of $U-O_{ax}$; (ii) a significantly decreasing intensity of peak B and increasing intensity of peak C indicated that oxygen atoms that were coordinated with uranyl ions from the water molecule were gradually replaced by the oxygen atoms from the nitrate ligand. Thus, the long distance of $U-O_{eq}(NO_3)$ increased the average $U-O_{eq}$ distance in uranyl nitrate solution with high HNO_3 concentrations.

The quantitative fitting results are listed in Table 1, and the fitted curves are plotted in Fig. 5(c). The obtained bond lengths of $U-O_{ax}$ were 1.77, 1.77, 1.77 and 1.76 Å for uranyl aqueous systems in solutions of 1 M $HClO_4$, 4 M HNO_3, 7 M HNO_3 and 10 M HNO_3, respectively. The obtained average bond lengths of $U-O_{eq}$ by EXAFS fits were 2.41, 2.43, 2.46 and 2.49 Å for uranyl aqueous systems in 1 M $HClO_4$, 4 M HNO_3, 7 M HNO_3 and 10 M HNO_3, respectively. Considering the experimental error of 0.02 Å for ΔR and 10–25% for ΔCN in EXAFS fits, the bond lengths and CN information obtained by EXAFS analysis were completely consistent with the XANES analysis, as shown in Figs. 6(a) and 6(b). This result indicated that the reported quantitative XANES analysis approach was reliable to extract local structural information in the uranyl complex.

3.4. Applications of XANES analysis

3.4.1. Application in other ubiquitous uranyl ligands. The aforementioned determined empirical equations could also be applied to other ubiquitous uranyl–ligands systems, such as carbonate and phosphate. For example, carbonate is a common anion found in many natural waters, and the complexation between carbonate and uranyl ions may play an important role in the migration of the uranium ion. In this study, we selected $(NH_4)_4UO_2(CO_3)_3$ powder as a representative of the uranyl–carbonate complex, and explored the applicability of XANES analysis in obtaining local structural
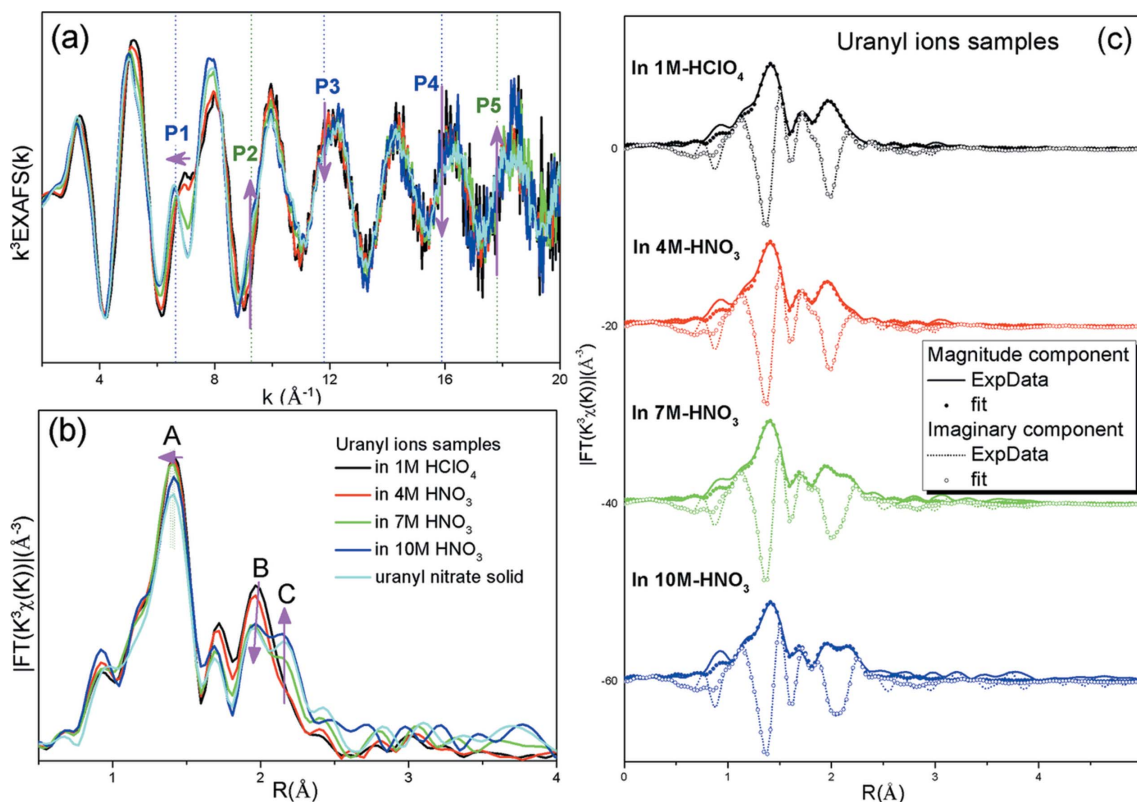
Figure 5
(a) The k-weighted EXAFS χ(k) function at the U L_3-edge for uranyl ions after subtracting the double-electron excitations in HClO$_4$, different concentrations HNO$_3$ solutions, and UO$_2$(NO$_3$)$_2$(H$_2$O)$_2$ solid powder. (b) Experimental FTs at the U L_3-edge for different uranyl complexes after subtracting the double-electron excitations. (c) Experimental magnitude and imaginary components of FTs at the U L_3-edge for different uranyl complexes and their corresponding fits.

Table 1
Structural parameters of uranyl ion at different nitrate concentrations from EXAFS fitting.

Sample	Bond type	CN	R (Å)	$\sigma^2 \times 10^{-3}$ (Å^2)	R-factor	Average R(U—O$_{eq}$)
UO$_2^{2+}$ in 1 M HClO$_4$	U—O$_{ax}$ U—O$_{eq}$	2 5 ± 0.2	1.77 ± 0.02 2.41 ± 0.02	1.5 ± 0.2 5.8 ± 0.5	0.01	2.41
UO$_2^{2+}$ in 4 M HNO$_3$	U—O$_{ax}$ U—O$_{eq}$(H$_2$O) U—O$_{eq}$(NO$_3$)	2 4.3 ± 0.4 1.3 ± 0.5	1.77 ± 0.02 2.41 ± 0.02 2.50 ± 0.02	1.4 ± 0.2 5.8 5.8	0.01	2.43
UO$_2^{2+}$ in 7 M HNO$_3$	U—O$_{ax}$ U—O$_{eq}$(H$_2$O) U—O$_{eq}$(NO$_3$)	2 2.3 ± 0.5 3.2 ± 0.4	1.77 ± 0.02 2.40 ± 0.02 2.51 ± 0.02	1.4 ± 0.1 5.8 5.8	0.01	2.46
UO$_2^{2+}$ in 10 M HNO$_3$	U—Oax U—O$_{eq}$(H$_2$O) U—O$_{eq}$(NO$_3$)	2 1.5 ± 0.4 4.4 ± 0.5	1.76 ± 0.02 2.40 ± 0.02 2.52 ± 0.02	1.7 ± 0.1 5.9 5.9	0.01	2.49

information. In Fig. 7(a), U L_3-edge XANES of (NH$_4$)$_4$UO$_2$-(CO$_3$)$_3$ was normalized and analysed by least-squares fitting, and the qualitative results of energy positions of peaks B and C are shown in Table S2. According to the XANES equation between R and XANES resonance features, the distances of U—O$_{ax}$ and U—O$_{eq}$ in (NH$_4$)$_4$UO$_2$(CO$_3$)$_3$ were approximately 1.80 ± 0.01 and 2.44 ± 0.01 Å, respectively. The results were exactly similar to the crystal data in previous reports (Serezhkin *et al.*, 1984; Graziani *et al.*, 1972), and also confirmed by EXAFS fitting (Fig. S6 and Table S1). Therefore,

it is a general argument that our XANES analysis can be used to explore the coordination distance in different uranyl complexes.

3.4.2. Application in low-concentration uranyl solution system. As previously mentioned, the XANES signal was stronger than that of EXAFS, so our established XANES analysis approach was more effective for the detection of low-concentration samples. Here we demonstrated the application of XANES analysis to explore the uranium local structure in a uranyl–amidoxime (AO) complex solution. AO-based absorbents exhibit superior uranium sequestering ability from seawater, in which the coordination structure of AO with uranyl have key roles (Tian *et al.*, 2012; Vukovic & Hay, 2013; Vukovic *et al.*, 2012; Barber *et al.*, 2012; Xu *et al.*, 2013) in designing highly selective and efficient materials. However, given the limitations of low uranium concentration in seawater and current synthesis technology, very limited information on the detailed local structure of the intrinsic UO$_2^{2+}$–AO complex is available. In this study, we prepared a UO$_2^{2+}$–AO solution with 40 p.p.m. uranium, which corresponded to very noisy EXAFS data shown in the inset of Fig. 7(b), thereby
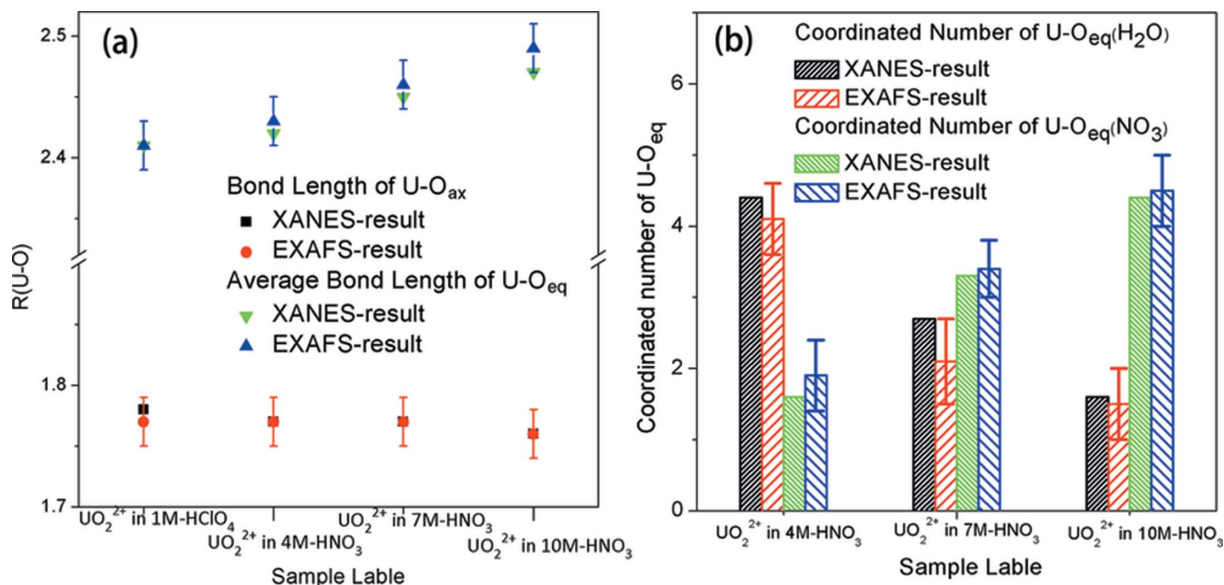
Figure 6
(*a*) Comparison of obtained bond length of U—O$_{ax}$ and U—O$_{eq}$ from XANES analysis and EXAFS fitting. (*b*) Comparison of obtained CN of U—O$_{eq}$ derived from the water molecule and nitrate ligand *via* XANES analysis and EXAFS fitting. (The uncertain values of EXAFS fitting are marked by error bars.)

making accurate EXAFS structural analysis impossible. By contrast, noticeable U L_3-edge XANES of the UO$_2$$^{2+}$–AO complex was the most available source of local structural information, which was normalized and analysed by least-squares fitting (Fig. 7*b*). The qualitative results of energy positions of peaks B and C are shown in Table S2. According to the linear relationship between the bond lengths and XANES features, the bond lengths of U—O$_{ax}$ and U—O$_{eq}$ in the UO$_2$$^{2+}$–AO complex were approximately 1.77 and 2.39 Å, respectively. These results were similar to those obtained by Vukovic *et al.* (2012), who reported that the distances of U—O$_{ax}$ and U—O$_{eq}$ in the UO$_2$(AO)$_2$(MeOH)$_2$ crystal are approximately 1.789 and 2.398 Å, respectively.

Similar quantitative approaches could be extended to other actinyl systems in spent fuel reprocessing (such as neptunyl

and plutonyl). The bipyramid structures of neptunyl and plutonyl are similar to that of uranyl. In their XANES spectra, two typical continuum resonance peaks were strongly correlated with the bond length of trans-dioxygen and equatorial ligands. Therefore, using the quantitative XANES relationship function, obtaining the local structural information for actinyl systems with extremely low concentrations becomes possible.

4. Conclusions

In summary, we conducted a systematic XAFS investigation around the uranium atom in several uranyl complexes. In a series of uranyl nitrate complexes, gradual changes in the U L_3-edge XANES were observed. Such changes contained a wealth of local geometric information. Combined with the MS
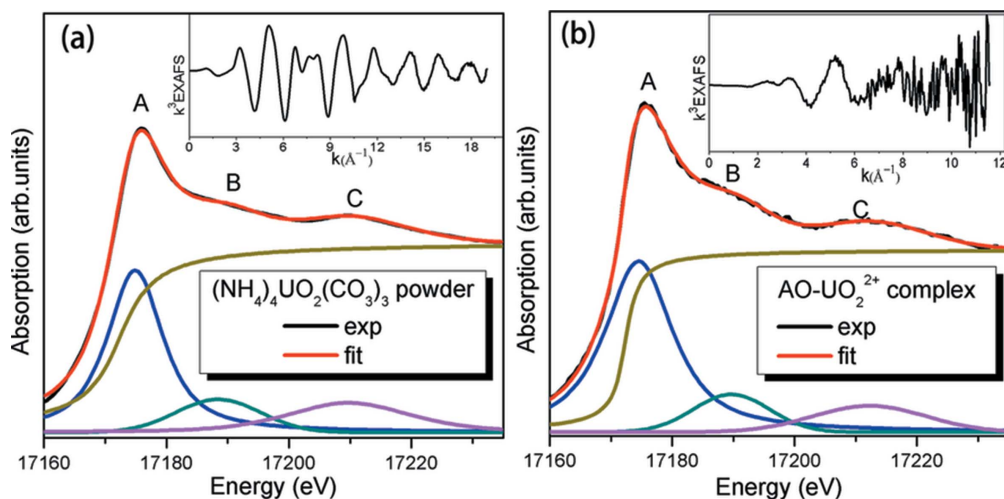

Figure 7
(*a*) Experimental U L_3-edge XANES spectra and their pseudo-Voigt line shapes by least-squares fitting in linear combination analyses for (NH$_4$)$_4$UO$_2$(CO$_3$)$_3$ powder. (*b*) Experimental U L_3-edge XANES spectra and their pseudo-Voigt line shapes by least-squares fitting in linear combination analyses for UO$_2$$^{2+}$–AO complex. The inset shows the corresponding *k*-weighted EXAFS $\chi(k)$ function.

calculation (*FEFF* code) and linear combination least-squares fit (*WinXAS*), we found that the energy positions of the XANES peaks in the uranyl solutions were closely related to the bond lengths R. Specifically, $1/R^2$ was proportional to ΔE, the difference between the MS resonance and WL. Thus, the quantitative bond length of $U-O_{ax}/O_{eq}$ and relative weight ratio of the equatorial oxygen ligand derived from the water molecule and nitrate ions were obtained. These obtained local structural data were further verified by the EXAFS fits. XANES analysis was used to obtain the local structure geometry for other uranyl complexes or solutions with extremely low U concentration when EXAFS oscillations could not be observed. This research is the first systematic study on uranyl chemistry *via* quantitative XANES analysis. In particular, this paper proposes a novel route to investigate other actinyl complexes (such as neptunyl and plutonyl).

References

Altmaier, M., Gaona, X. & Fanghänel, T. (2013). *Chem. Rev.* **113**, 901–943.

Bailey, E. H., Mosselmans, J. F. W. & Schofield, P. F. (2005). *Chem. Geol.* **216**, 1–16.

Barber, P. S., Kelley, S. P. & Rogers, R. D. (2012). *RSC Adv.* **2**, 8526–8530.

Benfatto, M. & Della Longa, S. (2001). *J. Synchrotron Rad.* **8**, 1087–1094.

Benfield, R. E., Filipponi, A., Bowron, D. T., Newport, R. J. & Gurman, S. J. (1994). *J. Phys. Condens. Matter*, **6**, 8429–8448.

Berto, S., Crea, F., Daniele, P. G., Gianguzza, A., Pettignano, A. & Sammartano, S. (2012). *Coord. Chem. Rev.* **256**, 63–81.

Bertram, S., Kaindl, G., Jové, J., Pagès, M. & Gal, J. (1989). *Phys. Rev. Lett.* **63**, 2680–2683.

Bianconi, A., Fritsch, E., Calas, G. & Petiau, J. (1985). *Phys. Rev. B*, **32**, 4292–4295.

Bugaev, L. A., Ildefonse, P., Flank, A. M., Sokolenko, A. P. & Dmitrienko, H. V. (1998). *J. Phys. Condens. Matter*, **10**, 5463–5473.

Bugaev, L. A., Ildefonse, P., Flank, A. M., Sokolenko, A. P. & Dmitrienko, H. V. (2000). *J. Phys. Condens. Matter*, **12**, 1119–1131.

Bugaev, L. A., Sokolenko, A. P., Dmitrienko, H. V. & Flank, A. M. (2001). *Phys. Rev. B*, **65**, 024105.

Bühl, M., Kabrede, H., Diss, R. & Wipff, G. (2006). *J. Am. Chem. Soc.* **128**, 6357–6368.

Chantler, C. T., Islam, M. T., Best, S. P., Tantau, L. J., Tran, C. Q., Cheah, M. H. & Payne, A. T. (2015). *J. Synchrotron Rad.* **22**, 1008–1021.

Chen, N., Kim, E., Arthur, Z., Daenzer, R., Warner, J., Demopoulos, G. P., Joly, Y. & Jiang, D. T. (2013). *J. Phys. Conf. Ser.* **430**, 012092.

Conradson, S. D., Abney, K. D., Begg, B. D., Brady, E. D., Clark, D. L., den Auwer, C., Ding, M., Dorhout, P. K., Espinosa-Faller, F. J., Gordon, P. L., Haire, R. G., Hess, N. J., Hess, R. F., Keogh, D. W., Lander, G. H., Lupinetti, A. J., Morales, L. A., Neu, M. P., Palmer, P. D., Paviet-Hartmann, P., Reilly, S. D., Runde, W. H., Tait, C. D., Veirs, D. K. & Wastin, F. (2004). *Inorg. Chem.* **43**, 116–131.

D'Angelo, P., Zitolo, A., Migliorati, V. & Persson, I. (2010). *Chem. Eur. J.* **16**, 684–692.

De Houwer, S. & Görller-Walrand, C. (2001). *J. Alloys Compd.* **323–324**, 683–687.

Den Auwer, C., Guillaumont, D., Guilbaud, P., Conradson, S. D., Rehr, J. J., Ankudinov, A. & Simoni, E. (2004). *New J. Chem.* **28**, 929–939.

Den Auwer, C., Simoni, E., Conradson, S. & Madic, C. (2003). *Eur. J. Inorg. Chem.* **2003**, 3843–3859.

Denecke, M. A. (2006). *Coord. Chem. Rev.* **250**, 730–754.

Denecke, M. A., Reich, T., Bubner, M., Pompe, S., Heise, K. H., Nitsche, H., Allen, P. G., Bucher, J. J., Edelstein, N. M. & Shuh, D. K. (1998). *J. Alloys Compd.* **271–273**, 123–127.

Gaillard, C., Klimchuk, O., Ouadi, A., Billard, I. & Hennig, C. (2012). *Dalton Trans.* **41**, 5476–5479.

Geckeis, H., Lützenkirchen, J., Polly, R., Rabung, T. & Schmidt, M. (2013). *Chem. Rev.* **113**, 1016–1062.

Gomilšek, J. P., Kodre, A., Arčon, I. & Hribar, M. (2003). *Phys. Rev. A*, **68**, 042505.

Graziani, R., Bombieri, G. & Forsellini, E. (1972). *J. Chem. Soc. Dalton Trans.* p. 2059.

Gückel, K., Tsushima, S. & Foerstendorf, H. (2013). *Dalton Trans.* **42**, 10172–10178.

Hagberg, D., Karlström, G., Roos, B. O. & Gagliardi, L. (2005). *J. Am. Chem. Soc.* **127**, 14250–14256.

Hennig, C. (2007). *Phys. Rev. B*, **75**, 035120.

Hennig, C., Schmeide, K., Brendler, V., Moll, H., Tsushima, S. & Scheinost, A. C. (2007). *Inorg. Chem.* **46**, 5882–5892.

Hennig, C., Tutschku, J., Rossberg, A., Bernhard, G. & Scheinost, A. C. (2005). *Inorg. Chem.* **44**, 6655–6661.

Hudson, E. A., Allen, P. G., Terminello, L. J., Denecke, M. A. & Reich, T. (1996). *Phys. Rev. B*, **54**, 156–165.

Hudson, E., Rehr, J. & Bucher, J. (1995). *Phys. Rev. B*, **52**, 13815–13826.

Ikeda, A., Hennig, C., Tsushima, S., Takao, K., Ikeda, Y., Scheinost, A. C. & Bernhard, G. (2007). *Inorg. Chem.* **46**, 4212–4219.

Ikeda-Ohno, A., Hennig, C., Rossberg, A., Funke, H., Scheinost, A. C., Bernhard, G. & Yaita, T. (2008). *Inorg. Chem.* **47**, 8294–8305.

Ikeda-Ohno, A., Hennig, C., Tsushima, S., Scheinost, A. C., Bernhard, G. & Yaita, T. (2009). *Inorg. Chem.* **48**, 7201–7210.

Jollivet, P., Auwer, C. D. & Simoni, E. (2002). *J. Nucl. Mater.* **301**, 142–152.

Joly, Y. (2001). *Phys. Rev. B*, **63**, 125120.

Jong, W. A. de, Aprà, E., Windus, T. L., Nichols, J. A., Harrison, R. J., Gutowski, K. E. & Dixon, D. A. (2005). *J. Phys. Chem. A*, **109**, 11568–11577.

Joseph, B., Iadecola, A., Fratini, M., Bianconi, A., Marcelli, A. & Saini, N. L. (2009). *J. Phys. Condens. Matter*, **21**, 432201.

Kaindl, G., Schmiester, G., Sampathkumaran, E. V. & Wachter, P. (1988). *Phys. Rev. B*, **38**, 10174–10177.

Kaindl, G., Wertheim, G. K., Schmiester, G. & Sampathkumaran, E. V. (1987). *Phys. Rev. Lett.* **58**, 606–609.

Kalkowski, G., Kaindl, G., Brewer, W. D. & Krone, W. (1987). *Phys. Rev. B*, **35**, 2667–2677.

Kalkowski, G., Kaindl, G., Wortmann, G., Lentz, D. & Krause, S. (1988). *Phys. Rev. B*, **37**, 1376–1382.

Kim, J., Tsouris, C., Mayes, R. T., Oyola, Y., Saito, T., Janke, C. J., Dai, S., Schneider, E. & Sachde, D. (2013). *Sep. Sci. Technol.* **48**, 367–387.

Knope, K. E. & Soderholm, L. (2013). *Chem. Rev.* **113**, 944–994.

Kodre, A., Arcon, I., Gomilsek, J. P., Preseren, R. & Frahm, R. (2002). *J. Phys. B*, **35**, 3497–3513.

Lee, P. A. & Pendry, J. B. (1975). *Phys. Rev. B*, **11**, 2795–2811.

Liu, X., Liu, H., Ma, H., Cao, C., Yu, M., Wang, Z., Deng, B., Wang, M. & Li, J. (2012). *Ind. Eng. Chem. Res.* **51**, 15089–15095.

Moulin, C., Decambox, P., Moulin, V. & Decaillon, J. G. (1995). *Anal. Chem.* **67**, 348–353.

Natoli, C. R. & Benfatto, M. (1986). *J. Phys. Colloq.* **47**, C8-1, 1–C823.

Natoli, C. R., Benfatto, M., Brouder, C., López, M. F. R. & Foulis, D. L. (1990). *Phys. Rev. B*, **42**, 1944–1968.

Pemberton, W. J., Droessler, J. E., Kinyanjui, J. M., Czerwinski, K. R. & Hatchett, D. W. (2013). *Electrochim. Acta*, **93**, 264–271.

Petiau, J., Calas, G., Petitmaire, D., Bianconi, A., Benfatto, M. & Marcelli, A. (1986). *Phys. Rev. B*, **34**, 7350–7361.

Polovov, I. B., Volkovich, V. A., Charnock, J. M., Kralj, B., Lewin, R. G., Kinoshita, H., May, I. & Sharrad, C. A. (2008). *Inorg. Chem.* **47**, 7474–7482.

Ravel, B. & Newville, M. (2005). *J. Synchrotron Rad.* **12**, 537–541.

Rehr, J. J., Kas, J. J., Vila, F. D., Prange, M. P. & Jorissen, K. (2010). *Phys. Chem. Chem. Phys.* **12**, 5503–5513.

Ressler, T. (1998). *J. Synchrotron Rad.* **5**, 118–122.

Sandström, M., Persson, I., Jalilehvand, F., Lindquist-Reis, P., Spångberg, D. & Hermansson, K. (2001). *J. Synchrotron Rad.* **8**, 657–659.

Schlegel, M. L. & Descostes, M. (2009). *Environ. Sci. Technol.* **43**, 8593–8598.

Serezhkin, V. N., Soldatkina, M. A. & Boiko, N. V. (1984). *J. Struct. Chem.* **24**, 770–774.

Shi, W.-Q., Yuan, L.-Y., Wang, C.-Z., Wang, L., Mei, L., Xiao, C.-L., Zhang, L., Li, Z.-J., Zhao, Y.-L. & Chai, Z.-F. (2014). *Adv. Mater.* **26**, 7807–7848.

Siboulet, B., Marsden, C. J. & Vitorge, P. (2006). *Chem. Phys.* **326**, 289–296.

Smolentsev, G. & Soldatov, A. (2006). *J. Synchrotron Rad.* **13**, 19–29.

Smolentsev, G. & Soldatov, A. V. (2007). *Comput. Mater. Sci.* **39**, 569–574.

Stöhr, J., Gland, J. L., Eberhardt, W., Outka, D., Madix, R. J., Sette, F., Koestner, R. J. & Doebler, U. (1983). *Phys. Rev. Lett.* **51**, 2414–2417.

Stoliker, D. L., Campbell, K. M., Fox, P. M., Singer, D. M., Kaviani, N., Carey, M., Peck, N. E., Bargar, J. R., Kent, D. B. & Davis, J. A. (2013). *Environ. Sci. Technol.* **47**, 9225–9232.

Templeton, D. H. & Templeton, L. K. (1982). *Acta Cryst.* A**38**, 62–67.

Tian, G., Teat, S. J., Zhang, Z. & Rao, L. (2012). *Dalton Trans.* **41**, 11579–11586.

Tyson, T. A., Hodgson, K. O., Natoli, C. R. & Benfatto, M. (1992). *Phys. Rev. B*, **46**, 5997–6019.

Visser, A. E., Jensen, M. P., Laszak, I., Nash, K. L., Choppin, G. R. & Rogers, R. D. (2003). *Inorg. Chem.* **42**, 2197–2199.

Vitova, T., Denecke, M. A., Göttlicher, J., Jorissen, K., Kas, J. J., Kvashnina, K., Prüßmann, T., Rehr, J. J. & Rothe, J. (2013). *J. Phys. Conf. Ser.* **430**, 012117.

Vitova, T., Kvashnina, K. O., Nocton, G., Sukharina, G., Denecke, M. A., Butorin, S. M., Mazzanti, M., Caciuffo, R., Soldatov, A., Behrends, T. & Geckeis, H. (2010). *Phys. Rev. B*, **82**, 235118.

Vukovic, S. & Hay, B. P. (2013). *Inorg. Chem.* **52**, 7805–7810.

Vukovic, S., Watson, L. A., Kang, S. O., Custelcean, R. & Hay, B. P. (2012). *Inorg. Chem.* **51**, 3855–3859.

Walshe, A., Prüßmann, T., Vitova, T. & Baker, R. J. (2014). *Dalton Trans.* **43**, 4400–4407.

Wu, Z. Y., Ouvrard, G., Moreau, P. & Natoli, C. R. (1997). *Phys. Rev. B*, **55**, 9508–9513.

Xu, C. F., Su, J., Xu, X. & Li, J. (2013). *Sci. Chin. Chem.* **56**, 1525–1532.

Xu, W., Chen, D., Chu, W., Wu, Z., Marcelli, A., Mottana, A., Soldatov, A. & Brigatti, M. F. (2011). *J. Synchrotron Rad.* **18**, 418–426.

Yang, F., Chu, W., Yu, M., Wang, Y., Ma, S., Dong, Y. & Wu, Z. (2008). *J. Synchrotron Rad.* **15**, 129–133.

Zhang, S., Zhang, L., Li, H., Li, J., Jiang, Z., Chu, W., Huang, Y., Wang, J. & Wu, Z. (2010). *J. Synchrotron Rad.* **17**, 600–605.

Zhang, X. W., Yan, X. J., Zhou, Z. R., Yang, F. F., Wu, Z. Y., Sun, H. B., Liang, W. X., Song, A. X., Lallemand-Breitenbach, V., Jeanne, M., Zhang, Q. Y., Yang, H. Y., Huang, Q. H., Zhou, G. B., Tong, J. H., Zhang, Y., Wu, J. H., Hu, H. Y., de Thé, H., Chen, S. J. & Chen, Z. (2010). *Science*, **328**, 240–243.